Article

A pendulum-based nanogenerator for high-entropy wave energy harvesting

Tiancong Zhao[1,2,4], Zhengyu Li[1,4], Bo Niu[1,4], Guangci Xie[1], Liang Shangguan[1], Meikun Zhang[1], Yurun Zhu [1], Yong Ma[1,3] ✉, Chao Hu[1] ✉ & Ying Li[2] ✉

As a fundamental component of marine technology development, the energy supply for unmanned oceanic equipment faces constraints imposed by traditional power generation methods. In-situ wave energy harvesting has recently garnered increasing attention. Here, we present a chaotic pendulum-based energy harvesting mechanism designed to efficiently capture high-entropy and broadband wave energy. This approach departs from the conventional reliance on resonance to enhance wave energy converter performance, instead enabling the conversion of disordered wave energy into regular mechanical energy. The tower-integrated generator design, combined with a charge-excitation circuit, enhances wave energy capture, achieving peak power densities of 56.7 W/m^3·Hz for the triboelectric nanogenerator and 192.3 W/m^3·Hz for the electromagnetic generator. A wireless monitoring system is developed and validated through water tank experiments and open-sea trials. This work offers strong support for extending the operational endurance of unmanned marine equipment and facilitating the advancement of oceanic energy solutions.

The monitoring, exploration, extraction, and maintenance of marine resources typically take place in remote offshore regions, necessitating distributed monitoring systems and networks capable of sustained long-term operation. Ensuring a reliable power supply while minimizing the operation and maintenance costs of communication systems, control units, and sensors, as well as achieving self-powered for deployed devices[1–3], has emerged as a pressing challenge demanding immediate attention. Consequently, the development and deployment of innovative, unmanned, intelligent, long-endurance, and cost-effective technologies and platforms have emerged as key focal areas in contemporary research and technological advancement[4–6]. Significantly, the in-situ harvesting of marine energy has been widely recognized by scholars as a promising solution to the endurance challenges confronting ocean monitoring systems[7–10]. Among marine renewable energy sources, wave energy exhibits distinct advantages, including abundant reserves, broad geographic distribution, and independence from diurnal cycle. Importantly, its power density

significantly exceeds that of wind and solar energy[11,12]. These inherent characteristics highlight its potential for continuous energy extraction, motivating extensive global research efforts. Researchers have proposed developing novel wave energy converters (WECs) to power distributed ocean monitoring buoys[13–15], further advancing the vision of marine energy utilization for diverse applications.

However, modern WEC technologies still face substantial challenges. These challenges include adaptability, energy capture efficiency, resonance bandwidth, and long-term operational reliability, which are key factors collectively hindering the commercialization of miniaturized WECs. Consequently, researchers have developed various advanced energy harvesting mechanisms to enhance the energy capture efficiency of WECs. Notably, the integration of nonlinear mechanisms and chaotic dynamic characteristics has emerged as a pivotal research focus. In terms of structural design, single pendulum[16,17], inverted pendulum[18], double pendulum[19], triple pendulum[20], and gimbal pendulum[21,22] have been utilized to enhance

[1]School of Ocean Engineering and Technology, Sun Yat-sen University, Guangzhou 510275, China. [2]Zhuhai Campus, Beijing Institute of Technology, Zhuhai 519088, P. R. China. [3]Southern Marine Science and Engineering Guangdong Laboratory (Zhuhai), Zhuhai 519000, China. [4]These authors contributed equally: Tiancong Zhao, Zhengyu Li, Bo Niu. ✉e-mail: mayong3@mail.sysu.edu.cn; huchao@hrbeu.edu.cn; bitliying@bit.edu.cn

WEC adaptability to multi-directional waves and improve performance in complex sea conditions. This rotational pendulum-based mechanism shifts the traditional thinking of enhancing WEC performance via frequency resonance effects. Instead, it leverages wave steepness excitation to enable the internal pendulum to rotate adaptively within the floater[23], thereby simplifying the control system and enhancing high-entropy wave energy capture. However, this approach presents new challenges, as these mechanisms exhibit substantial mechanical complexity and constrained load-bearing capacity, rendering them suitable only for generators with simplified structures and lightweight designs. Further, the inherent simplicity and weight limitations of these structures constrain their power output, leading to a performance bottleneck. Thus, the development of power generation systems compatible with these mechanisms is urgently required to enhance the operational longevity of marine monitoring equipment.

Currently, the most commonly utilized power generation technologies include piezoelectric generator (PG), electromagnetic generator (EMG), and triboelectric nanogenerator (TENG) technologies[24]. PGs generally feature an elastomeric structure that deforms in response to wave loads, thereby driving the power generation unit. However, the low output power and limited service life of this technology hinder its development. EMGs are generally known for their high-frequency output but often come with large structural dimensions and substantial weight. Guo et al.[25] designed an eccentric fan-shaped pendulum to capture wave energy, which is subsequently transmitted through an integrated gearbox mechanism to drive the EMG. Wave tank experiments demonstrated that the device's output power density could reach 0.24 mW/cm³. To harness ultra-low-frequency wave energy, Li et al.[26] developed a spherical single-pendulum WEC that utilizes low-frequency waves to drive a gearbox, facilitating high-speed rotation of the EMG rotor. When the peak wave heights exceed 0.6 m, the device can generate up to 0.13 W of power, which is sufficient to operate most low-power components. Wang et al.[27] proposed an unanchored drifting buoy with an EMG system, incorporating two orthogonally arranged eccentric rings that perform hoop-like motions during operation. The power generation system has a mass of 3.5 kg, accounting for ~3% of the buoy's total weight. A prototype of the WEC was then developed. Tests revealed that its output power could reach 0.56 W when the buoy's primary frequency ranged between 0.7 and 1.0 Hz. In summary, WECs present a viable solution for providing sustainable power to buoys. However, the characteristic constraints of EMGs often necessitate larger carrier platforms to counteract the adverse effects of pendulum motion, including mass center shifts and asymmetric mass distribution, which ultimately diminish primary energy conversion efficiency.

TENGs are distinguished by their high efficiency at low frequencies, simple structures, and lightweight design[28–30]. In wave energy applications, TENGs are mainly classified based on their operating modes, including contact-separation mode[31,32], rolling-freestanding layer mode[33], and sliding mode[34,35]. The contact-separation mode, characterized by its simple structure, typically utilizes arch-shaped or spring-supported configurations. These researcher-developed structures excel in harvesting high-frequency and large-amplitude wave energy. Among the various TENGs, the rolling freestanding-layer TENG circumvents electrostatic shielding effects, with tower-like and arc-shaped configurations being evolutions of this concept[36]. These designs greatly improve the long-term stability of TENGs by minimizing direct friction between the contact surfaces. However, a critical limitation arises from the restricted effective contact area between dielectric layers, leading to suboptimal charge transfer and diminished power output. Additionally, the inertial ball inside the device weakens the wave-induced motion response, functioning in a manner akin to a tuned mass damper (TMD)[37], which often requires stronger external excitations in real marine environments (such as waves exceeding 0.5 m in height or wind speeds surpassing 9 m/s)[38]. In contrast, the rotary

pendulum-type TENG leverages sliding mode to significantly increase the effective contact area of dielectric layers[39–41], enabling faster charge transfer rates and prolonged retention within a two-dimensional plane while maintaining low mechanical complexity. Based on potential energy storage/release strategy, Cao et al.[42] introduced a TENG featuring a swing-rotation switching mechanism to efficiently capture low-frequency mechanical energy (0.3 ~ 5 Hz). This design achieves a bandwidth 4 times broader than that of traditional cylindrical pendulum TENGs, with peak power densities of 10.1 W/m³ at 1.8 Hz and 15.4 W/m³ at 5 Hz. However, the need to maintain stable floater oscillations typically requires miniaturization of the power generation system, fundamentally limiting potential output power enhancement.

Consequently, the integration of rotary pendulum-type TENG with the rolling freestanding-layer architectures presents a viable strategy to circumvent the power output limitations of WECs while maintaining operational stability. Theoretically, this approach is quite feasible, particularly when further combined with electromagnetic generation. Chen et al.[43] proposed a chaotic pendulum hybrid nanogenerator combining TENG and EMG with optimized power management circuits, demonstrating effective wave energy scavenging for autonomous wireless sensor networks. Experimental results revealed power outputs of 15.21 μW (TENG) and 1.23 mW (EMG), with data transmission over 300 m, offering a novel solution for energy harvesting. Han et al.[44] features a hybrid nanogenerator with double-sided fluff fabric structure. This design enhances space utilization and achieves maximum power densities of 2.02 W/m³ for TENG and 16.96 W/m³ for EMG, exhibiting superior performance at ultra-low frequencies. Such hybrid systems deliver enhanced power output with improved conversion efficiency alongside the combined advantages of TENGs and EMGs. These improvements enable reliable in-situ energy supply for distributed marine monitoring networks while exhibiting strong commercialization potential in offshore applications.

In this work, we present a chaotic pendulum-based triboelectric-electromagnetic hybrid wave energy converter (CP-TEWEC), which integrates a double-pendulum chaotic system to decouple the floater from the internal generator (Supplementary Note 1). This design efficiently transforms high-entropy wave energy into stable rotational mechanical energy while preserving buoy stability. The hybrid TENG-EMG system achieves remarkable peak power densities of 56.7 W/m³·Hz (TENG) and 192.3 W/m³·Hz (EMG), representing 28.3 folds and 11.3 folds improvements over Han's work, respectively. We further propose a novel charge excitation circuit, which enhances the generator's energy storage capacity by 4.6 folds compared to conventional DB107 rectifier-based circuit. Additionally, an ultra-low-power self-powered marine sensor system is developed for wireless temperature/humidity monitoring. Notably, the buoy's performance is rigorously validated under irregular waves in controlled tank tests and real-sea trials, demonstrating reliable self-powered operation and wireless data transmission, which fulfilling the energy autonomy requirements of distributed marine monitoring networks. By synergizing chaotic mechanics with hybrid energy harvesting, this work establishes a design paradigm for high-efficiency small-scale WECs and expands the functionality frontier of marine Internet of Things (MIoT)-compatible WECs.

Results
Configuration and working mechanism
Figure 1a illustrated a three-dimensional schematic of the CP-TEWEC buoy under realistic oceanic deployment conditions. Upon wave excitation, the chaotic pendulum (Fig. S1) mechanism initially transforms irregular wave-induced motion into constrained oscillations of the tray pendulum (Fig. 1c) about its pivot axis, followed by conversion into regular rotation of the rotary pendulum (Fig. 1b), thereby mechanically driving the generator. The decoupling mechanism (Supplementary Movie S1, Note S1 and Fig. 1f) isolates the
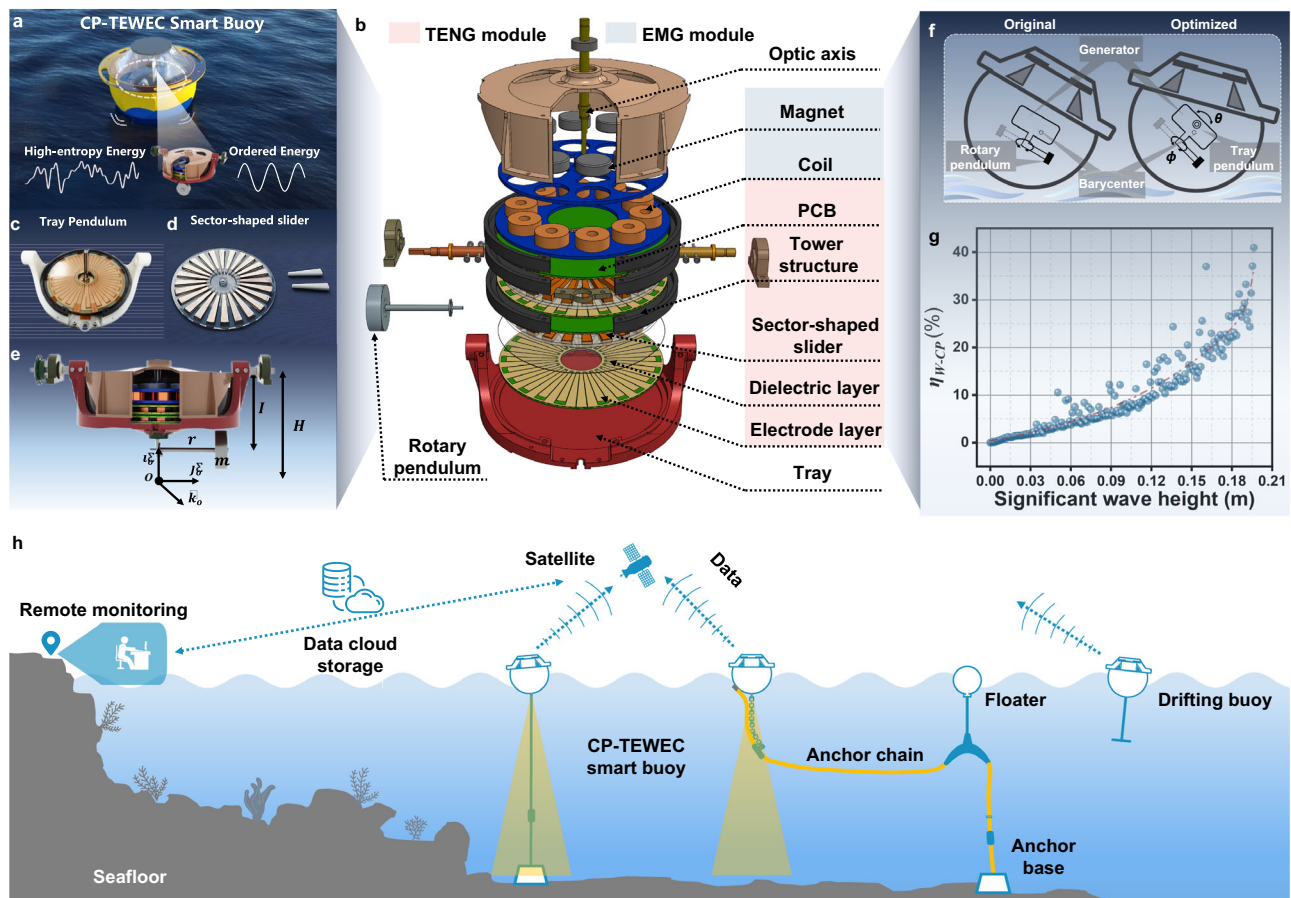
Fig. 1 | Application scenario and scheme design of the CP-TEWEC. a Schematic of the CP-TEWEC applied in high-entropy wave energy harvesting. **b** The internal view of the device structure. The tray pendulum (**c**), slide mode sector-shaped slider (**d**), and corresponding psychical model (**e**) of chaotic pendulum adopted in this work. **f** Comparison of the CP-TEWEC buoy's working mechanism using a chaotic pendulum versus a rotary pendulum. **g** Simulated results showing the average energy conversion efficiency from wave energy to chaotic pendulum mechanical energy under different significant wave heights. **h** Potential application scenario of the proposed CP-TEWEC buoy.

generator's motion from the buoy's oscillations, stabilizing the generator's barycenter relative to the buoy frame and guaranteeing steady operational output. Simultaneously, the buoy achieves adaptive equilibrium in the water, harnessing high-entropy wave energy to power its onboard equipment. To quantify the chaotic pendulum's high-entropy wave energy capability, we established a physical model (Fig. 1e and Fig. S2) integrating multi-body coupling dynamics. Using Lagrangian mechanics, we formulated electro-mechanical coupled governing equations (Supplementary Note 2) and evaluated the CP-TEWEC's energy capture efficiency under stochastic wave forcing. Figure 1g reveals that across the spectral peak period ($0 < T_p < 5\,s$), the wave-to-mechanical conversion efficiency ($\eta_{W\text{-}CP}$) peaks at 41% for $H_s = 0.196\,m$, with $\eta_{W\text{-}CP}$ scaling monotonically with significant wave height (H_s). This result addresses the traditional limitations of low energy conversion efficiency typically observed in miniaturized WECs. Detailed derivations and calculations are provided in Supplementary Note 2, 3.

The hybrid nanogenerator integrates two complementary energy conversion modules, consisting of a TENG capable of generating high-voltage and an EMG that delivers sustained high currents. The EMG architecture (Fig. 1b) incorporates ten axially embedded sets of metal coils and permanent magnets. These coils are connected in series to increase voltage output. Figure 1d illustrates the TENG rotor, featuring a hub-style acrylic outer rotor and 24 sector-shaped inner rotors. Each inner rotor is manufactured by acrylonitrile butadiene styrene (ABS) material via fused deposition modeling (FDM) 3D printing, and its

surface is laminated with copper foil. Additionally, a gap is maintained between the inner and outer rotors, while the stators and the outer rotor constrain the inner rotors within specific sectors. This setup allows the inner rotors to rotate under the influence of gravity, producing rotational friction with the dielectric layer. This results in an adequate frictional contact area for effective charge generation, while also significantly reducing the rotor's startup torque. As illustrated in Supplementary Fig. S3, the TENG stator comprises a printed circuit board (PCB) and a tower structure. To ensure optimal contact area between the TENG stator and rotor, the number of pole pairs N for the metal inner and outer electrodes (i.e., grid count) is set to 24 pairs. The CP-TEWEC system architecture (Fig. 1h) demonstrates dual functionality as both WEC and self-powered MIoT platform. It is envisioned to serve as either an anchored platform or a drifting buoy, integrating advanced functionalities, including surface and underwater monitoring, navigational alerts, wireless data transmission, and environmental sensing.

We conducted Multiphysics finite element analysis (COMSOL v6.1) on both magnetic field (Rotating Machinery Module) and electrostatic (Electrostatics Module) simulations to evaluate their performance (Supplementary Note 4, 5 detail the simulation process). Figure 2a displays the parameterized EMG unit geometry, with critical component annotated. Owing to the symmetric geometry of the EMG module, only 1/10 of the full geometry requires analysis, which allows computational efficiency. By means of the sector symmetry and periodic boundary condition functions in the FEA software, the full 3D
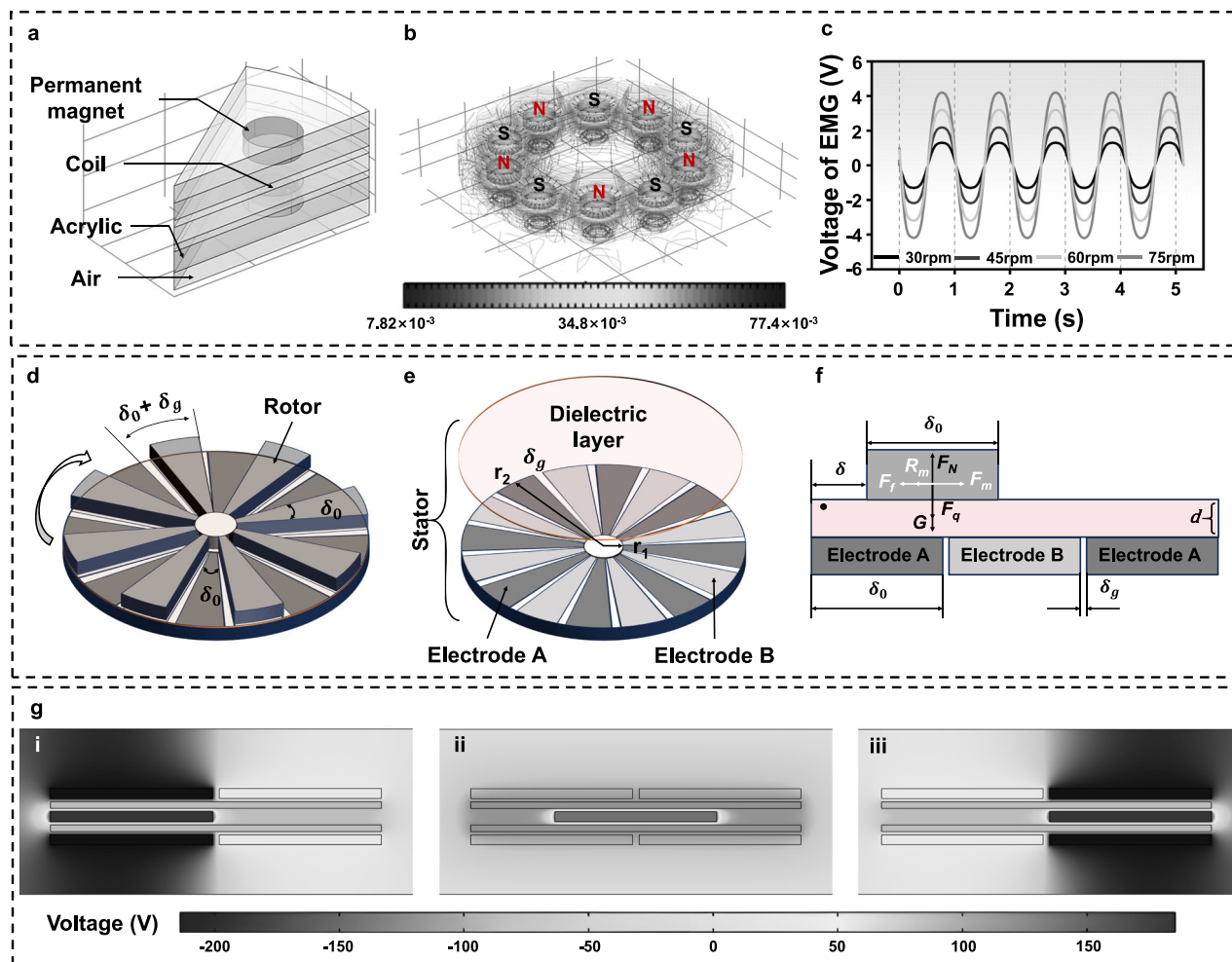
Fig. 2 | The working principle and output characteristics of the CP-TEWEC. Schematic of the EMG model (**a**) and its magnetic flux density (**b**). **c** Simulation of the EMG voltage with diverse rotation speed using COMSOL. Schematic of the TENG rotor (**d**) and stator (**e**). **f** Mechanical model of the TENG. **g** Simulation of the potential difference across the electrodes under open-circuit conditions using COMSOL.

simulation results of the EMG module can be accurately reconstructed. The magnetic flux density distribution of the EMG module, reconstructed from a 3D sector dataset, is depicted in Fig. 2b. The color gradient quantifies flux density magnitude, where field line density (contour interval of 0.05 T) correlates with local energy conversion potential. This model confirms speed-independent flux characteristics, achieving a peak flux density of 758 mT. As illustrated in Fig. 2c, transient simulations employing dynamic mesh refinement characterized the EMG's voltage generation across operational speeds (30 - 75 rpm in 15 rpm increments), establishing critical foundations for experimental validation. The geometric parameters of the TENG module are detailed in Fig. 2d, e. Under electrostatic principles, the TENG is modeled as fully charged via triboelectric contact. To simplify model, we assume a uniform charge distribution over an infinite plane, with zero-potential reference at infinity. The potential difference between electrodes A and B is derived as follows[45],

$$V_{oc} = \frac{4d\sigma}{\varepsilon_0 \varepsilon_r} \tag{1-1}$$

where ε_0 and ε_r denote the vacuum permittivity and relative permittivity of the dielectric layer, respectively. d and σ are the thickness and charge density of dielectric layer. From Eq. (1-1), the peak-to-peak open-circuit voltage of the TENG over a single rotation cycle can be determined. The voltage-charge relationship across electrodes A and B

is derived using a variable capacitor model,

$$V_{AB} = -\frac{Q_{AB}}{C_{AB}} + V_{oc} \tag{1-2}$$

C_{AB} represents the interelectrode capacitance, and Q_{AB} is the accumulated charge. The short-circuit transferred charge between electrodes A and B is calculated from the rotor-electrode overlapping area, as follows,

$$Q_{sc} = \frac{\delta_0}{180°} \sigma \boldsymbol{\pi} (r_2^2 - r_1^2) \tag{1-3}$$

δ_O is the grid angle of metal electrode. r_1 and r_2 denotes the inner and outer diameters of the electrodes. Thus, the theoretical maximum output of the TENG module, derived from Eqs. (1-1–1-3), enables the preliminary selection of materials and structural parameters. Figure 2f illustrates that the rotational damping of the generator rotor is influenced by multiple factors, including the slider-weight-induced friction, triboelectrically driven electrostatic adhesion, electromagnetic reluctance, aerodynamic drag, and eddy current dissipation. Based on Ruyter's theory[46], the electrostatic adhesion force generated at the

slider-dielectric interface is given by,

$$F_q = \frac{Q_\delta^2}{\varepsilon_0 \varepsilon_r S} = \frac{\sigma^2 \boldsymbol{\pi}(r_2^2 - r_1^2)}{\varepsilon_0 \varepsilon_r} \qquad (1\text{-}4)$$

In this equation, Q_δ corresponds to the total triboelectric charge accumulated at the slider-dielectric interface, with S defining the effective contact area. During stator-rotor relative rotation, electrostatic adhesion forces inevitably introduce additional resistance to the motion of the sector-shaped sliding blocks. To minimize energy dissipation, we optimized the slider mass to balance triboelectric contact pressure while mitigating inertial and frictional losses. Energy loss arises from microscale interfacial friction, inducing asperity deformation, lattice dislocations, and phonon-mediated thermal dissipation. Eq. (1-4) reveals that the electrostatic adhesion force is rotationally invariant, governed exclusively by the dielectric material's charge density (σ), interfacial geometry (r_1, r_2), and intrinsic triboelectric properties. Further, the coreless EMG module further enhances low-speed energy harvesting via a contactless design, eliminating mechanical wear and eddy current losses. Thus, the damping model simplifies to a rotationally aligned friction term, neglecting secondary effects from air resistance and eddy currents,

$$f = \mu \left(m_s g + \frac{\sigma^2 \boldsymbol{\pi}(r_2^2 - r_1^2)}{\varepsilon_0 \varepsilon_r} \right) + \frac{L_s}{\mu_0 S_l} \qquad (1\text{-}5)$$

In this equation, μ denotes the coefficient of friction between the slider and the dielectric layer, m_s represents the total mass of all sliders, L_s indicates the magnetic circuit length of the electromagnetic module, μ_0 signifies the relative permeability in air, and S_l denotes the cross-sectional area of the magnetic circuit. From Eq. (1-5) and Table S1 parameters, the maximum static friction ($F_s = f$) reaches 3.5 N, defining the critical threshold for pendulum motion initiation. Consequently, the pendulum mass (m_p) must satisfy $m_p > 0.357$ kg to overcome F_s. Figure 2g (i-iii) show a measured potential difference ($V_{exp} = 430$ V), agreeing within 7.9% of the theoretical V_{oc} (466.67 V, Eq. 1-1). This deviation can be attributed to assumptions in the theoretical model, such as uniform charge distribution and idealized material properties. Despite these simplifications, the small discrepancy between the two results confirms the reliability of both the theoretical and simulation approaches.

Performance evaluation

To validate the hybrid nanogenerator's electromechanical model and power generation characteristic, we tested its electrical output using the custom test platform in Fig. 3a. Figure 3b quantifies the TENG's AC output across rotational speeds (30 - 75 rpm in 15 rpm increments), revealing speed-dependent trends in voltage and current. The V_{oc} stabilizes near 649 V across all speeds, with a < 10% decline at 75 rpm (Fig. 3b), suggesting minor charge leakage or inertial effects at higher velocities. The observed reduction arises from centrifugal-force-induced partial levitation of the fan-shaped sliders, which decreases the effective dielectric contact area by counteracting gravity. The TENG's short-circuit current (I_{sc}) scales linearly with rotational speed, peaking at 80 μA (75 rpm), confirming triboelectric charge transfer rate dependence on interfacial separation frequency. Figure 3c demonstrates EMG's Faraday-law-governed response that both V_{oc} and I_{sc} exhibit ω-proportionality, with peak outputs of 4.15 V and 109 mA at 75 rpm. To maximize energy extraction, we designed a charge extraction circuit (CEC, Fig. 3d) that synchronizes with the TENG's cycles. At 60 rpm and load resistance $R_l = 7$ MΩ, the CEC-augmented TENG achieves a 233.8 μA current pulse (Fig. 3e), delivering 0.1 J in 5 s. Figure 3f reveals the CEC's power optimization. At $R_l = 7$ MΩ, the TENG hits peak efficiency (20 mW avg., 0.2 W peak), outperforming rectifier bridges (DB107) by 22.5 folds in charge

density (Fig. S4). Capacitor charging tests (Fig. 3g) confirm the CEC's 4.6 folds rate enhancement, attributable to reduced charge recombination during energy transfer phases. The EMG's matched-load power (0.19 W at $R_l = 51$ Ω, 60 rpm, Fig. 3h) underscores its high-frequency advantage, complementing the TENG's low-frequency dominance. This frequency-selective synergy expands the hybrid nanogenerator's operational bandwidth, boosting comprehensive power by 51.2% relative to standalone modules. Figure 3i characterizes the EMG's capacitive charging dynamics across capacitances ($C = 22 - 330$ μF), revealing C-dependent energy storage profiles. At 60 rpm, the EMG charges a 22 μF capacitor to 3 V in 0.2 s (initial $dV/dt = 15$ V/s), transitioning to linear growth (1.5 V/s) upon approaching saturation. For higher capacitances (47 - 330 μF), the EMG maintains rapid initial charging (2 V in <0.3 s), though with progressive rate attenuation. Therefore, a capacitance of 22 μF is more suitable for the EMG module. After over 10^6 cycles, the PVC dielectric layer is sampled, with its surface morphology and surface potential images captured. Fig. S5 corroborates the TENG's operational robustness, with post-cycling morphological homogeneity (<15% variation, initial 130 nm) and higher potential output.

Wave tank experiments

To quantify the buoy's energy harvesting performance under controlled hydrodynamic conditions, we developed a precisely instrumented wave tank platform. Figure 4a details the wave tank's 2D experimental configuration, including buoy placement relative to wave generators and sensors for irregular wave testing. Fig. S6 provides a field-view of the smart buoy's deployment, illustrating its free-floating orientation in operational conditions. Wave gauge measurements (Fig. 4b) captured characteristic sea states with a spectral peak period (T_p) of 1.94 s and significant wave height (H_s) of 0.114 m, replicating realistic ocean wave. Figures 4c, d and S7 characterize the coupled electromechanical response, showcasing pendulum kinematics, EMG current, and TENG voltage under irregular wave excitation. The pendulum's 11.75 rad/s motion (112 rpm peak rotation speed, Fig. S8) drives concurrent energy conversion that EMG delivers peak current of 78 mA while TENG generates peak voltage of 560 V, confirming dual-mode harvesting efficacy. This further validates that the chaotic pendulum mechanism effectively converts high-entropy wave energy into orderly rotational motion, successfully driving the generator. Data in Fig. 4e demonstrate that the average output power of the TENG module reaches its peak across different spectral peak periods at a load of 7 MΩ. Specifically, at a spectral peak period of 1.9 s, the average output power density of the TENG module is measured at 15.8 W/m³·Hz, while its peak output power density reaches 56.7 W/m³·Hz. In addition, the EMG module exhibits an average output power density of 32.7 W/m³·Hz (Fig. 4f) and a peak output power density of 192.3 W/m³·Hz. It is noted that near the spectral peak period of 1.9 s, both the TENG and EMG modules exhibit a significant surge in output power. This phenomenon can be attributed to the inherent period of the designed buoy being 1.92 s (see Fig. S9). Also, the RAO response of the buoy under regular wave (Fig. S10) conditions also supports this view. Interestingly, at $T_p = 1.2$ s, both generators outperform resonance conditions (TENG, +14.4%; EMG, +8.3%) due to increased buoy tilt amplitude ($\psi = 21.3°$ vs 14° at 1.9 s), enhancing mechanical excitation (Fig. S11). As shown in Fig. 4g, the comparison of $\eta_{W\text{-}CP}$ values obtained from numerical calculations and wave tank experiments demonstrates high consistency between the two data sets, confirming the validity of the numerical calculation method.

Figure 4h benchmarks the hybrid system against 10 prior designs (2016 - 2023), showing this work improvements over state-of-the-art WECs. The output power density of the TENG module in this study significantly surpasses that of previous research, potentially due to the advantages of its rotational tower structure. Compared to previous similar collectors, the EMG module has also made significant
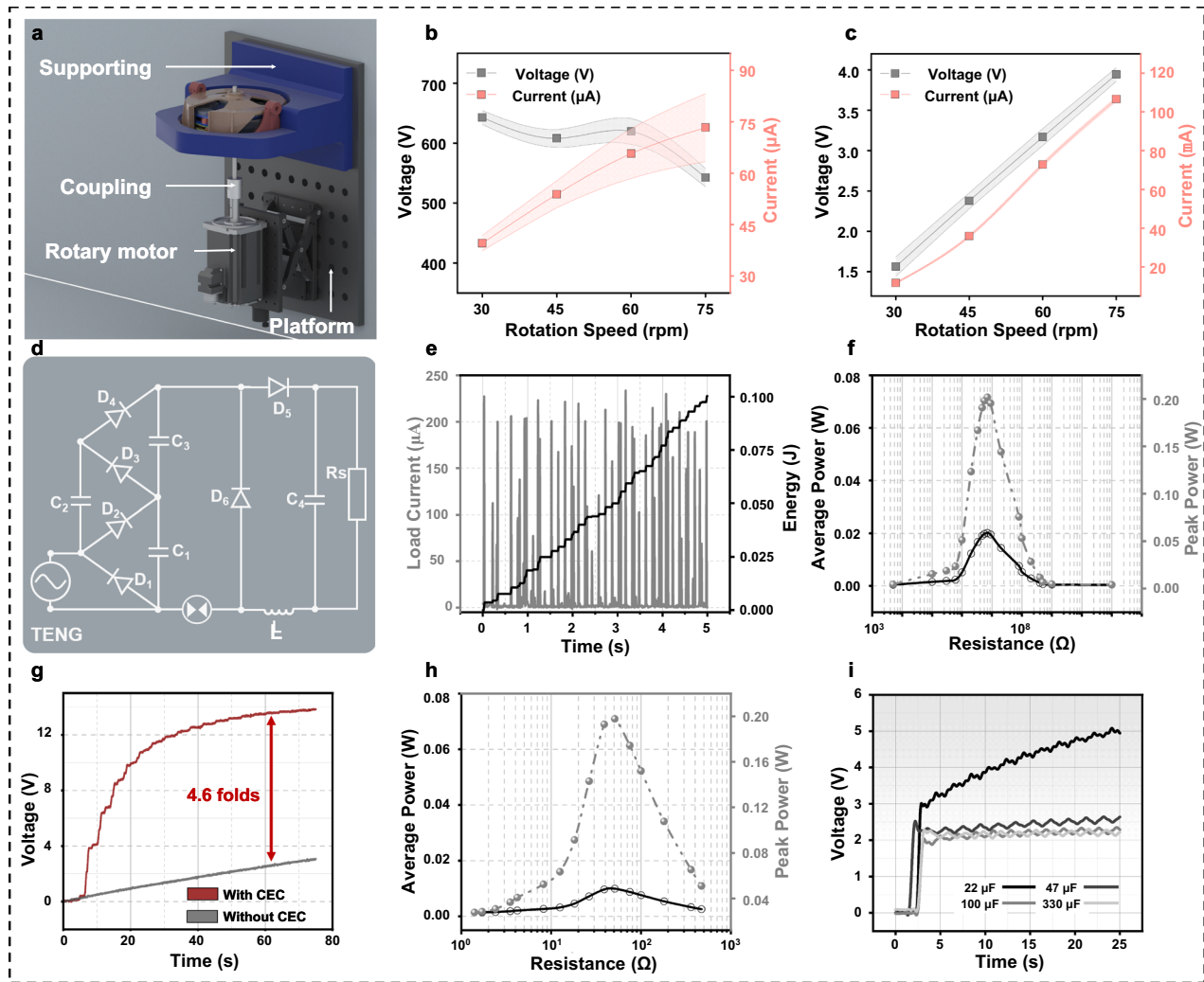
Fig. 3 | The output performance of the CP-TEWEC under regular rotating excitation. a Schematic of the rotating excitation test system. The average voltage and current for the TENG (**b**) and EMG (**c**) under different rotation speed. **d** The schematic charge excitation circuit (CEC) diagram of the TENG. **e** The load current and accumulated energy with single TENG unit under 60 rpm. **f** The average power and peak power of single TENG unit under 60 rpm. **g** Comparison of the capacitor (47 μF) charging speeds of the TENG with and without CEC. **h** The average power and peak power of EMG under 60 rpm. **i** The charging characteristic curves of EMG using full-rectifying-bridge for different capacitors.

advancements in output power density, thanks to the design of the chaotic pendulum mechanism. This mechanism enables the coil to more effectively and stably capture the magnetic field variations induced by rotational motion. The high output power density of the CP-TEWEC makes it suitable for a monitoring buoy, efficiently harnessing wave energy. With a wave-to-wire efficiency of 5.21% (Supplementary Note 6), the CP-TEWEC could generate 144 Wh/day, which would be sufficient to autonomously power oceanographic buoys while lowering maintenance costs compared to conventional WECs.

Demonstration of application in marine environments

Although the variable-speed motion of the rotating pendulum enhances energy harvesting efficiency, it simultaneously induces fluctuations in the generator's output voltage and current, thereby compromising the stability of its power delivery. To mitigate this issue, we designed a voltage regulation circuit with integrated energy management and storage capabilities. As shown in Fig. 5a, the system employs a low-power integrated chip (LTC3588), where the generator's direct current output is connected to PZ1 and PZ2, while capacitor C serves as the energy storage buffer, ensuring consistent power output under dynamic mechanical inputs.

The integration of a power management circuit enables the hybrid nanogenerator to continuously power temperature and humidity sensors, as demonstrated in Supplementary Movie S2. Under irregular wave conditions (T_p = 1.9 s, H_s = 0.12 m), the generator module's output voltage stabilizes at 5 V shortly after activation (Fig. S12a). Further testing across varying spectral peak periods (Fig. S12b) confirms that the LTC3588-based energy management circuit ensures robust output stability, significantly reducing power fluctuations. This system efficiently converts harvested wave energy into regulated outputs capable of driving low-power devices, including navigational lights and wireless sensors (Fig. 5b, c and Supplementary Movie S3). To validate real-world performance, the circuit module, comprising a rectification circuit, power management unit, and wireless sensor, was sealed within the CP-TEWEC buoy's energy management chamber (Fig. S13). Field tests conducted at the deployment site (Fig. 5d, S14) under average conditions (wind speed, 0.93 m/s; wave period, 1.93 s; wave height, 0.1 m) confirmed reliable operation, demonstrating the system's suitability for sustained oceanographic monitoring. As demonstrated in Fig. 5e, f and Supplementary Movie S4, the CP-TEWEC buoy achieves full operational capability within 30 s of wave-induced oscillation. Upon activation, the system wirelessly transmits temperature
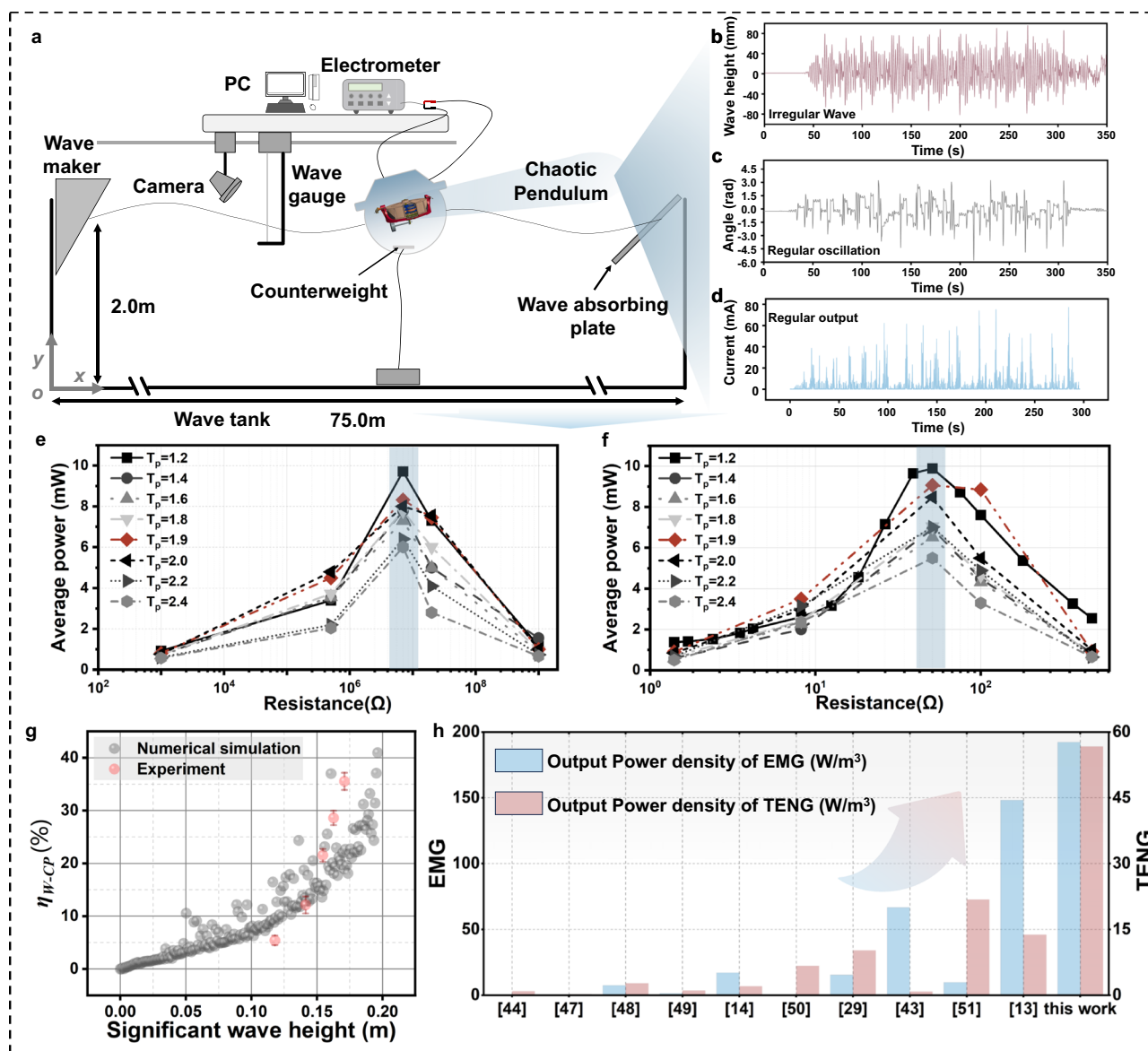
Fig. 4 | Performance of CP-TEWEC buoy under irregular waves. a Distribution of experimental tests in float water tanks. **b**–**d** CP-TEWEC buoy energy conversion spectrum. The average power of TENG (**e**) and EMG (**f**) with diverse resistance under irregular wave excitation. **g** The comparison of $\eta_{W\text{-}CP}$ between numerical simulation and experimental results. **h** Comparison of the power density between this study and other hybrid nanogenerator for harvesting wave energy[13,14,29,43,44,47–51].

and humidity data to a shore-based PC (over 292 m), enabling real-time environmental monitoring. This successful field validation under authentic marine conditions confirms the buoy's ability to simultaneously harvest wave energy and power wireless telemetry, demonstrating a practical solution to extend the operational endurance of autonomous monitoring systems.

Discussion

In this study, we design and prototype a highly integrated chaotic pendulum-based triboelectric-electromagnetic hybrid wave energy harvester tailored for self-powered buoys. The chaotic pendulum is encapsulated within the float to ensure high reliability, effectively converting external high-entropy wave energy into the stable rotational motion of the pendulum while integrating the TENG and the EMG. This integration expands the operational bandwidth of the generator and achieves effective complementary output characteristics between the two systems. The design of the hub-type rotor structure realizes the seamless integration of the TENG and the EMG, providing enhanced start-up performance. By optimizing the structure

and integrating grating electrodes with CEC to improve the generator's performance, we undertook a thorough investigation into the operational principles and performance characteristics of the proposed hybrid nanogenerator. With this design, the CP-TEWEC can generate an instantaneous power density of 249 W/m³·Hz and an average power density of 48.5 W/m³·Hz under irregular wave conditions, demonstrating its efficient wave energy harvesting capability. The output of the CP-TEWEC buoy significantly surpassed that of previously published composite generators, enabling it to easily power navigation lights and various sensing devices.

Additionally, a low-power wireless monitoring system is developed for remote and wireless marine environmental monitoring. Meanwhile, the CP-TEWEC buoy achieved in-situ wave energy supply, as validated under both dry and sea trial conditions. In sea trials, the self-powered buoy successfully demonstrated real-time environmental monitoring, completing data transmission within 30 s over a 292 m range. This work showcases, to the best of our knowledge, a rare practical implementation of a chaotic pendulum based triboelectric-electromagnetic hybrid nanogenerator for autonomous marine
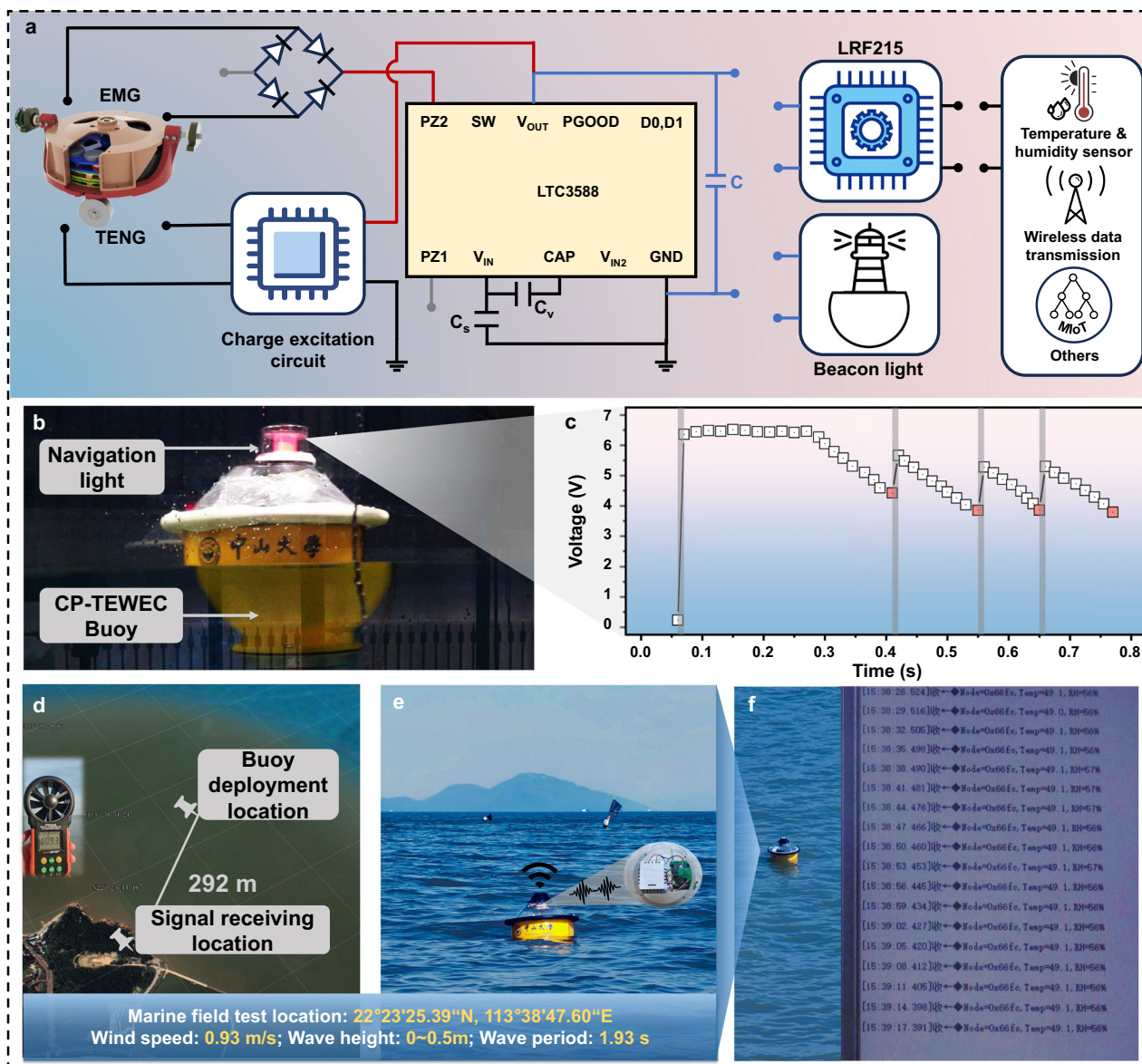
Fig. 5 | Application demonstration of the CP-TEWEC buoy. a Design of energy management circuit. The CP-TEWEC buoy lights up navigational lights (**b**) and the voltage variation (**c**) of capacitor. The location arrangement of the receiver (**d**) and the buoy (**e**). **f** The illustration of the transmission signal on PC.

sensing under realistic wave conditions, highlighting its potential for sustainable ocean monitoring. Compared to conventional WECs, the CP-TEWEC system exhibits superior power density, conversion efficiency and robustness against wave-impact loads, making it particularly suitable for powering miniaturized distributed sensors in MIoT applications. This design advances the industrial feasibility of small-scale WECs, offering a pathway toward marine energy-self-sufficient digital twin applications.

Methods
Fabrication of the TENG
The outer rotor has an outer diameter of 150 mm and an inner diameter of 8 mm. It consists of 48 fan-shaped electrodes, grouped into 24 electrode pairs (sectors), each spanning 7° with an inter-electrode gap of 0.5°. The corresponding chord length for each electrode is 52.5 mm, ensuring full 360° coverage around the rotor. The height of the central flange structure is 5.5 mm, while the hub height measures 3 mm, and a radial positioning hole for the optical axis has a diameter of 3 mm. Each inner rotor weighs 1.5 g, has an angle of 6.5°, a chord

length of 50 mm, and a height of 5.5 mm. For the base material, polylactic acid (PLA) is chosen, and copper foil tape is adhered to the surface. The PCB is made from a composite material consisting of epoxy resin and fiberglass, with a thickness of 1.6 mm and copper electrodes that are 35 μm thick. The tower, constructed from nylon, features cutouts at the output terminals of the internal and external electrodes to facilitate the wiring of the TENG generating unit. Additionally, three threaded through-holes are integrated into the tower to ease the integration and securing of multiple generating units.

A single TENG unit comprises a set of TENG rotors, a PCB, and a dielectric layer. The assembly process consists of the following steps: (1) The outer rotor of the TENG hub is manufactured using a laser cutter (XTOOL F1 Ultra) with acrylic as the material. (2) The sliding inner rotor within the TENG sector is produced using an FDM 3D printer (A8S) with ABS as the material. (3) Copper foil tape is adhered to the sliding components within the sectors. (4) The PCB, dielectric film, and tower are secured in place using Kapton tape. (5) The outer rotor is fixed onto the optical axis, and the inner rotor is inserted into the outer rotor hub, thereby completing the assembly.

Components of the CEC

The CEC consists of two components: the rectification section and the charge excitation section. The rectification section converts the AC output from the rotating tower-type TENG to DC output through a full-bridge rectifier (DB107). The charge excitation section, which is the core of the CEC, regulates the voltage and impedance of the generator. Capacitors C1, C2 and C3 (10 kV, 1000 pF) is used for boosting voltage. C4 serve as direct loads for the TENG module, optimizing energy extraction during the charging phase. The gas discharge tube (SX51-150) acts as a switch, allowing the capacitors to accumulate energy under low-frequency excitation and release it instantly. The remaining components include a fast recovery diode (MUR460) and an inductor rated at 10 mH.

Components of the self-powered ocean monitoring system

The components of the self-powered ocean monitoring system include a chaotic pendulum triboelectric electromagnetic hybrid generator, a CEC, charging capacitors, a voltage regulator (LTC3588), communication equipment, and a laptop. The capacitors gather power from the generating unit and connect to the voltage regulator. The communication equipment comprises a wireless module, a serial port module, an external antenna, and an energy supply module. The wireless and serial modules use the LRF215 communication module, while the main control chip, CC2530F256, operates in an ultra-low power mode, drawing only 2 μA in low power operation. This configuration guarantees that when the storage capacitors accumulate enough energy, the system can perform a quick cold start, ensuring continued operation even if the voltage falls within tolerance limits.

Fabrication of the buoy

In the experiments, a full-scale (1:1) prototype was used to ensure that the experimental conditions closely resemble real-world marine environments. All structural parameters, including dimensions, mass distribution, and hydrodynamic properties, were maintained identical to those of the actual deployed system. This approach eliminates scale effects that may arise in reduced-scale models, ensuring that the experimental results accurately reflect the device's real-world performance. The measured parameters in this study, such as wave-induced motion, power generation efficiency, and structural stability, therefore correspond directly to the full-scale system.

The CP-TEWEC buoy consists of several key components: a float, an energy management chamber, a chaotic pendulum, and a ballast chamber. The experimental model weighs 10 kg and has a diameter of 0.43 m and a height of 0.46 m. The float features a spherical shell constructed from a closed-cell material with a density of 0.1 g/cm^3. For ballast, six circular lead weights, each weighing 0.5 kg, are integrated into the buoy's ballast chamber. A polymer material is sprayed onto the surface of the float to ensure its water tightness and reliability, while also improving its visual appearance.

The tray pendulum is mounted inside the buoy's cavity, with the optical axis affixed to the tray pendulum, extending downward and connecting to the rotating pendulum. The self-powered ocean monitoring system is positioned within the energy management chamber, with the sensor probe situated at the top of the buoy and sealed with a waterproof connector.

Characterization and measurement

The Keithley 6514 electrometer (sampling frequency of 1 kHz) is utilized to measure the electrical output characteristics of the generator, which are displayed through a customized LabVIEW VI application. Atomic force microscopy (Cypher-ES) is used to scan the surface topography and surface potential of the PVC film, and the probe model is ASYELEC-01-R2 (1.42 nN·nm^{-1}). A rotating motor (BXM-6400) provides simple rotational excitation to evaluate the generator's

performance. A digital inclinometer (YGQ300-D model, sampling frequency ranging from 1 Hz to 50 Hz) is employed for free decay tests in still water, as well as for assessing the buoy's response to wave excitation. A hollow shaft angular displacement sensor (WKA-D22-B model) measures the swing angle, angular velocity, and angular acceleration of both the tray and rotating pendulums, allowing for unrestricted continuous rotation and aiding in measuring the pendulum's motion response to wave stimulation. A digital wave height gauge (YWH200-DXX model) records the actual wave heights and periods under both regular and irregular wave conditions. The dynamic signal testing and analysis platform (DHDAS Model) also operates at a sampling frequency of 1 kHz, recording the response angles of the buoy, tray oscillation angle, and rotational pendulum angle in real-time using a hollow angular displacement sensor.

The specialized wave tank (Fig. S15), which can simulate both regular and irregular wave excitations, are 75 m in length, 2 m in height, and 1.6 m in width. The wave height gauge is positioned 5 m in front of the model and measures 0.2 m below the still water surface to determine the speed and height of incoming waves. Waves are generated by a wave maker located on the left side of the towing tank, which consists of a gearbox and a variable-speed motor to precisely control the wedge-shaped wave block for accurate hydrodynamic conditions. The water depth is maintained at 0.965 m, with the positive flow direction designated as the x-axis and the perpendicular wave direction as the y-axis, while the outward normal to the x-o-y plane represents the z-axis. The buoy is deployed in the optimal measurement zone at coordinates ($x = 50$ m, $y = 0.8$ m), which serves as the reference point for all instrument locations and movements. A total of 30 irregular wave conditions were established, with each condition consisting of 150 wave cycles. The average duration of each wave generation was 7 min, with spectral peak periods ranging from 1.1 s to 2.6 s and significant wave heights between 0.08 m and 0.18 m.

Data availability

The Source data generated in this study are provided in the Supplementary Information. Any additional requests for information can be directed to and will be fulfilled by the corresponding authors. Source data are provided with this paper.

References

1. Wang, Z. L. Triboelectric nanogenerators as new energy technology for self-powered systems and as active mechanical and chemical sensors. *ACS Nano* **7**, 9533 (2013).
2. Wang, Z. L. Triboelectric nanogenerators as new energy technology and self-powered sensors - principles, problems and perspectives. *Faraday Discuss* **176**, 447–458 (2014).
3. Wu, C., Wang, A. C., Ding, W., Guo, H. & Wang, Z. L. Triboelectric nanogenerator: a foundation of the energy for the new era. *Adv. Energy Mater.* **9**, 1802906 (2019).
4. Kroger, S. & Law, R. J. Sensing the sea. *Trends Biotechnol.* **23**, 250–256 (2005).
5. Albaladejo, C. et al. Wireless sensor networks for oceanographic monitoring: a systematic review. *Sens* **10**, 6948–6968 (2010).
6. Zhao, T. et al. Recent progress in blue energy harvesting for powering distributed sensors in ocean. *Nano Energy* **88**, 106199 (2021).
7. Schiermeier, Q., Tollefson, J. & Scully, T. Electricity without carbon. *Nature* **454**, 816–823 (2008).
8. Tollefson, J. Power from the oceans: blue energy. *Nature* **508**, 302–304 (2014).
9. Scruggs, J. & Jacob, P. Harvesting ocean wave energy. *Science* **323**, 1176–1178 (2009).
10. Wang, Q., Qiu, Z., Yang, S., Li, H. & Li, X. Design and experimental research of a novel deep-sea self-sustaining profiling float for observing the northeast off the luzon island. *Sci. Rep.* **12**, 18885 (2022).

11. Falcão, A. F. & de, O. Wave energy utilization: a review of the technologies. *Renew. Sustain. Energy Rev.* **14**, 899–918 (2010).
12. Wang, Z. L., Jiang, T. & Xu, L. Toward the blue energy dream by triboelectric nanogenerator networks. *Nano Energy* **39**, 9–23 (2017).
13. Hong, H. et al. Self-powered seesaw structured spherical buoys based on a hybrid triboelectric–electromagnetic nanogenerator for sea surface wireless positioning. *Energy Environ. Sci.* **15**, 621–632 (2022).
14. Ahmed, A. et al. Design of an S-shaped point-absorber wave energy converter with a non-linear PTO to power the satellite-respondent buoys in the East China Sea. *Ocean Eng.* **275**, 114162 (2023).
15. Zhang, C. et al. Hybridized triboelectric-electromagnetic nanogenerators for efficient harvesting of wave energy for self-powered ocean buoy. *Nano Energy* **128**, 109929 (2024).
16. Lenci, S., Brocchini, M. & Lorenzoni, C. Experimental rotations of a pendulum on water waves. *J. Comput. Nonlinear Dyn.* **7**, 11007 (2012).
17. Jiang, X. et al. System analysis and experimental investigation of a pendulum-based wave energy converter. *Ocean Eng.* **277**, 114300 (2023).
18. Wu, J. et al. Investigation on the wave energy converter that reacts against an internal inverted pendulum. *Energy* **247**, 123493 (2022).
19. Kumar, R., Gupta, S. & Ali, S. F. Energy harvesting from chaos in base excited double pendulum. *Mech. Syst. Signal Process.* **124**, 49–64 (2019).
20. Alevras, P., Brown, I. & Yurchenko, D. Experimental investigation of a rotating parametric pendulum. *Nonlinear Dyn.* **81**, 201–213 (2015).
21. Sequeira, D., Little, J. & Mann, B. P. Investigating threshold escape behavior for the gimballed horizontal pendulum system. *J. Sound Vib.* **450**, 47–60 (2019).
22. Wang, T., Lou, H. & Zhu, S. Bandwidth enhancement of a gimbaled-pendulum vibration energy harvester using spatial multi-stable mechanism. *Appl. Energy* **326**, 120047 (2022).
23. Reid, M., Sorokin, V. & Aw, K. Effects of pendulum orientation and excitation type on the energy harvesting performance of a pendulum based wave energy converter. *Nonlinear Dyn.* **112**, 20755–20769 (2024).
24. Wang, Z. L. Nanogenerators, self-powered systems, blue energy, piezotronics and piezo-phototronics – a recall on the original thoughts for coining these fields. *Nano Energy* **54**, 477–483 (2018).
25. Guo, Q. *et al*. Design and experiment of an electromagnetic ocean wave energy harvesting device. in *2018 IEEE/ASME International Conference on Advanced Intelligent Mechatronics (AIM)* 381–384 (IEEE, Auckland, New Zealand, 2018).
26. Li, Y. et al. Study of an electromagnetic ocean wave energy harvester driven by an efficient swing body toward the self-powered ocean buoy application. *IEEE Access* **7**, 129758–129769 (2019).
27. Wang, Y.-J. & Lee, C.-K. Dynamics and power generation of wave energy converters mimicking biaxial hula-hoop motion for mooring-less buoys. *Energy* **183**, 547–560 (2019).
28. Zhao, H. et al. Underwater wireless communication via TENG-generated Maxwell's displacement current. *Nat. Commun.* **13**, 3325 (2022).
29. Wang, X. et al. Fully packaged blue energy harvester by hybridizing a rolling triboelectric nanogenerator and an electromagnetic generator. *ACS Nano* **10**, 11369–11376 (2016).
30. Cheng, T., Shao, J. & Wang, Z. L. Triboelectric nanogenerators. *Nat. Rev. Methods Prim.* **3**, 39 (2023).
31. Liang, X. et al. Spherical triboelectric nanogenerator integrated with power management module for harvesting multidirectional water wave energy. *Energy Environ. Sci.* **13**, 277–285 (2020).
32. Xi, F. et al. Self-powered intelligent buoy system by water wave energy for sustainable and autonomous wireless sensing and data transmission. *Nano Energy* **61**, 1–9 (2019).
33. Wang, X. et al. Triboelectric nanogenerator based on fully enclosed rolling spherical structure for harvesting low-frequency water wave energy. *Adv. Energy Mater.* **5**, 1501467 (2015).
34. Wen, Z. et al. Harvesting broad frequency band blue energy by a triboelectric–electromagnetic hybrid nanogenerator. *ACS Nano* **10**, 6526–6534 (2016).
35. Bai, Y. et al. High-performance triboelectric nanogenerators for self-powered, in-situ and real-time water quality mapping. *Nano Energy* **66**, 104117 (2019).
36. Xu, M. et al. High power density tower-like triboelectric nanogenerator for harvesting arbitrary directional water wave energy. *ACS Nano* **13**, 1932–1939 (2019).
37. Lu, Z., Wang, Z., Masri, S. F. & Lu, X. Particle impact dampers: past, present, and future. *Struct. Control Health Monit.* **25**, e2058 (2018).
38. Zhu, C. et al. Highly integrated triboelectric-electromagnetic wave energy harvester toward self-powered marine buoy. *Adv. Energy Mater.* **13**, 2301665 (2023).
39. Li, T. et al. Bidirectional rotating turbine hybrid triboelectric-electromagnetic wave energy harvester for marine environment monitoring. *Adv. Energy Mater.* **14**, 2400313 (2024).
40. Jiang, T., Chen, X., Han, C. B., Tang, W. & Wang, Z. L. Theoretical study of rotary freestanding triboelectric nanogenerators. *Adv. Funct. Mater.* **25**, 2928–2938 (2015).
41. Lin, L. et al. Segmentally structured disk triboelectric nanogenerator for harvesting rotational mechanical energy. *Nano Lett.* **13**, 2916–2923 (2013).
42. Cao, B. et al. Broadband and output-controllable triboelectric nanogenerator enabled by coupling swing-rotation switching mechanism with potential energy storage/release strategy for low-frequency mechanical energy harvesting. *Adv. Energy Mater.* **12**, 2202627 (2022).
43. Chen, X. et al. A chaotic pendulum triboelectric-electromagnetic hybridized nanogenerator for wave energy scavenging and self-powered wireless sensing system. *Nano Energy* **69**, 104440 (2020).
44. Han, C. et al. Hybrid triboelectric-electromagnetic nanogenerator with a double-sided fluff and double Halbach array for wave energy harvesting. *Adv. Funct. Mater.* **32**, 2205011 (2022).
45. Zhu, G., Chen, J., Zhang, T., Jing, Q. & Wang, Z. L. Radial-arrayed rotary electrification for high performance triboelectric generator. *Nat. Commun.* **5**, 3426 (2014).
46. Shao, J. et al. Studying about applied force and the output performance of sliding-mode triboelectric nanogenerators. *Nano Energy* **48**, 292–300 (2018).
47. Jung, H., Ouro-Koura, H., Salalila, A., Salalila, M. & Deng, Z. D. Frequency-multiplied cylindrical triboelectric nanogenerator for harvesting low frequency wave energy to power ocean observation system. *Nano Energy* **99**, 107365 (2022).
48. Ouyang, R., Huang, Y., Ye, H., Zhang, Z. & Xue, H. Copper particles-PTFE tube based triboelectric nanogenerator for wave energy harvesting. *Nano Energy* **102**, 107749 (2022).
49. Zhang, Q. et al. High performance liquid-solid tubular triboelectric nanogenerator for scavenging water wave energy. *Nano Energy* **103**, 107810 (2022).
50. Wang, J. et al. Rational structure optimized hybrid nanogenerator for highly efficient water wave energy harvesting. *Adv. Energy Mater.* **9**, 1802892 (2019).
51. Yawei, F. et al. Soft-contact cylindrical triboelectric-electromagnetic hybrid nanogenerator based on swing structure for ultra-low frequency water wave energy harvesting. *Nano Energy* **81**, 105625 (2021).

Acknowledgements

Author contributions

Y.M., Y.L. and C.H. supervised and guided the project; T.Z., Z.L., and B.N. conceived the idea and designed the experiments. G.X., L.S., and M.Z. optimized the TENG's configuration and manufacturing methods; T.Z., Z.L., B.N., L.S., M.Z., and Y.Z. fabricated the harvester and performed the experiments; T.Z. and Z.L. designed and fabricated the auxiliary circuits.

Competing interests

The authors declare no competing interests.

Additional information

Supplementary information The online version contains supplementary material available at
https://doi.org/10.1038/s41467-025-60443-8.

Correspondence and requests for materials should be addressed to Yong Ma, Chao Hu or Ying Li.

Peer review information *Nature Communications* thanks Tao Jiang, and the other, anonymous, reviewers for their contribution to the peer review of this work. A peer review file is available.

Reprints and permissions information is available at
http://www.nature.com/reprints

Publisher's note Springer Nature remains neutral with regard to jurisdictional claims in published maps and institutional affiliations.